Accelerated Short-TE 3D Proton Echo-Planar Spectroscopic Imaging Using 2D-SENSE with a 32-Channel Array Coil

Ricardo Otazo,[1*] Shang-Yueh Tsai,[2] Fa-Hsuan Lin,[3–5] and Stefan Posse[1,6,7]

MR spectroscopic imaging (MRSI) with whole brain coverage in clinically feasible acquisition times still remains a major challenge. A combination of MRSI with parallel imaging has shown promise to reduce the long encoding times and 2D acceleration with a large array coil is expected to provide high acceleration capability. In this work a very high-speed method for 3D-MRSI based on the combination of proton echo planar spectroscopic imaging (PEPSI) with regularized 2D-SENSE reconstruction is developed. Regularization was performed by constraining the singular value decomposition of the encoding matrix to reduce the effect of low-value and overlapped coil sensitivities. The effects of spectral heterogeneity and discontinuities in coil sensitivity across the spectroscopic voxels were minimized by unaliasing the point spread function. As a result the contamination from extracranial lipids was reduced 1.6-fold on average compared to standard SENSE. We show that the acquisition of short-TE (15 ms) 3D-PEPSI at 3 T with a $32 \times 32 \times 8$ spatial matrix using a 32-channel array coil can be accelerated 8-fold ($R = 4 \times 2$) along y-z to achieve a minimum acquisition time of 1 min. Maps of the concentrations of N-acetyl-aspartate, creatine, choline, and glutamate were obtained with moderate reduction in spatial-spectral quality. The short acquisition time makes the method suitable for volumetric metabolite mapping in clinical studies. Magn Reson Med 58:1107–1116, 2007. © 2007 Wiley-Liss, Inc.

Key words: echo-planar spectroscopic imaging; parallel imaging; SENSE; regularization; large array coil

MR spectroscopic imaging (MRSI) provides spatial distribution of chemical shifts (1,2). As traditionally imple-

mented with phase-encoding (3), it is very time-consuming, requiring as many repetitions as there are voxels in the image, e.g., the acquisition time for a 3D experiment is given by $T_A = N_x N_y N_z T_R$, where N_x, N_y, and N_z are the dimensions of the spatial grid and TR is the repetition time. As a consequence, MRSI is usually restricted to low spatial resolution and single-slice acquisition in clinical practice. The development of fast MRSI methods that enable whole brain coverage with high spatial resolution remains a major challenge in MRSI research. Many methods have been developed to provide faster spatial-spectral encoding (4), such as echo-planar techniques that allow for simultaneous spatial-spectral encoding using time-varying gradients (5). Proton echo planar spectroscopic imaging (PEPSI) (6,7) is an implementation of this technique with a trapezoidal readout gradient for simultaneous encoding of one spatial dimension (x) and the spectral dimension (f) providing a net acceleration of N_x over the conventional phase-encoding method with comparable signal-to-noise ratio (SNR) per unit time and unit volume (8). However, 3D-PEPSI is still very time-consuming due to phase-encoding along the third spatial dimension.

Accelerated spatial encoding can be accomplished using parallel imaging techniques (9,10), where subsampled k-space data are acquired using multiple receive coils with spatially varying reception profiles. The knowledge of the spatially varying coil sensitivity profiles allows for reconstruction of subsampled data. Acceleration is obtained at the expense of SNR reduction in the reconstructed image. Sensitivity-encoding (SENSE) (11) parallel imaging method has been applied to accelerate phase-encoded (12) and turbo-spin-echo (TSE) MRSI (13). Even though SENSE reconstruction is applied in the same way as in MRI for each spectral point of the MRSI data, the low-resolution characteristics of the MRSI acquisition can produce residual aliasing artifacts if the coil sensitivities vary within the voxel. In order to reduce these artifacts Dydak et al. (12) used extrapolation of the sensitivity maps to avoid discontinuities at the border; Zhao et al. (14) employed a two-step SENSE reconstruction to optimize the sensitivity maps; and Sanchez-Gonzalez et al. (15) proposed using coil sensitivities with higher spatial resolution to optimize the point spread function (PSF) with respect to variation of the coil sensitivities within a voxel. Using 2D SENSE with TSE-MRSI, Dydak (16) has shown 3D-MRSI within 20 min with a 2×2 acceleration along x and y using a $32 \times 32 \times 8$ spatial matrix. Further acceleration in parallel MRSI can be obtained by combining fast gradient-encoding techniques such as echo-planar encoding and parallel imaging. We recently introduced the combination of 1D-SENSE and 2D-PEPSI using an array coil with eight elements to

[1]Electrical and Computer Engineering Department, University of New Mexico, Albuquerque, New Mexico.

[2]Department of Electrical Engineering, National Taiwan University, Taipei, Taiwan.

[3]MGH-HMS-MIT Athinoula A. Martinos Center for Biomedical Imaging, Charlestown, Massachusetts.

[4]Department of Radiology, Massachusetts General Hospital, Boston, Massachusetts.

[5]Institute of Biomedical Engineering, National Taiwan University, Taipei, Taiwan.

[6]Department of Psychiatry, University of New Mexico School of Medicine, Albuquerque, New Mexico.

[7]Department of Physics and Astronomy, University of New Mexico, Albuquerque, New Mexico.

*Correspondence to: Ricardo Otazo, Electrical and Computer Engineering Department, University of New Mexico, MSC01 1100 ECE Bldg., Albuquerque, NM 87131. E-mail: otazo@ece.unm.edu

achieve up to 3-fold acceleration along the *y* dimension (17). We also presented preliminary data using the combination of 1D-GRAPPA (generalized autocalibrating partially parallel acquisition) and PEPSI in previous studies obtaining a similar acceleration factor (18,19). Recently, Zhu et al. (20) demonstrated an acceleration factor of 1.5 using 1D-GRAPPA and 3D-EPSI.

Acceleration in parallel imaging is limited by the available SNR and the spatially varying noise amplification factor in the reconstruction (g-factor). Several methods were proposed to reduce the loss in SNR in order to achieve higher accelerations, such as acceleration along more than one spatial dimension (e.g., 2D-SENSE (21)) and the use of very high field scanners, which increases the baseline SNR and also improves sensitivity encoding by taking advantage of the stronger spatial modulation of the coil profiles (22). Other works have described the adaptation of the array coil geometry to minimize g-factor (23), regularization in the reconstruction to improve conditioning of the encoding matrix (24), and array coils with a large number of small elements to increase sensitivity and disparate coil sensitivity encoding along all spatial dimensions (25,26).

The use of 2D acceleration combined with an array coil with a large number of elements is expected to provide high acceleration capability for 3D encoding. For example, acceleration factors as high as 16 were demonstrated in in vivo for imaging experiments using 32-element arrays designed for multidimensional sensitivity encoding (25,26). Moreover, in contrast to single surface coils, large array coils also provide an improved depth penetration for volumetric applications (27,28).

This work aims at developing a very high speed encoding method for volumetric spectroscopic imaging in human brain at short TE using a combination of 3D-PEPSI and regularized 2D-SENSE reconstruction. High 2D-acceleration factors were feasible using a 32-element array coil. To overcome the technical challenges of this implementation we use regularization of the inverse matrix problem to reduce amplification of noise and coil sensitivity estimation errors in positions with low-value and overlapped coil sensitivities, and optimization of the sensitivity maps to avoid residual aliasing artifacts due to the low spatial resolution nature of MRSI. This is particularly important for minimizing contamination from peripheral lipids due to increased residual aliasing of the PSF with high acceleration. Lipid contamination is particularly strong at short TE, which is advantageous for maintaining the sensitivity gain at high field, as metabolite T_2-values have been shown to decrease with field strength (29,30). We demonstrate the feasibility of 3D-MRSI at 3 T in 1 min for a $32 \times 32 \times 8$ spatial matrix and 0.7 cc nominal voxel size.

MATERIALS AND METHODS

Data Acquisition

3D-PEPSI measurements were performed on healthy volunteers using a 3T MR scanner (Tim Trio, Siemens Medical Solutions, Erlangen, Germany) equipped with Sonata gradients (maximum amplitude: 40 mT/m, slew rate: 200 mT/m/ms). The scanner has a built-in 32-channel RF
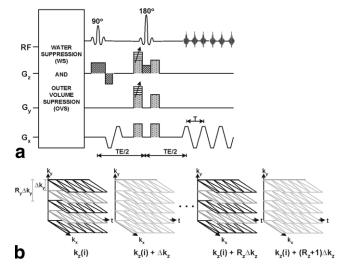

FIG. 1. **a:** 3D-PEPSI pulse sequence with water-suppression (WS), outer-volume-suppression (OVS), spin-echo RF excitation, phase encodes on G_y and G_z for *y* and *z* encoding and trapezoidal G_x gradient for simultaneous encoding of *x* and *f*. **b:** The resulting *k*-space trajectory is composed by parallel planes of zig-zag k_x-*t* trajectories. Δk_y and Δk_z determine the uniform sampling grid for k_y and k_z. The black lines represents the trajectory after downsampling k_y and k_z by a factor R_y and R_z, respectively.

receiver capability. A noncommercially available 32-channel head array coil (31) was used for RF reception, while RF transmission was performed with a quadrature body coil. The receiver array coil was built with a close-fitting helmet design with circular elements arranged in patterns of hexagonal and pentagonal symmetry similar to a soccer ball providing sensitivity encoding along all spatial directions and higher sensitivity at any depth when compared to commercial 8-channel array coils (31).

The 3D-PEPSI sequence (6) consisted of water-suppression (WS), outer-volume-suppression (OVS), spin-echo RF excitation, phase-encoding for *y* and *z,* and the echo-planar readout module (Fig. 1). WS was performed using a 3-pulse WET module (32). OVS was applied along the perimeter of the brain using 14 slices: 8 slices were manually positioned in the axial plane and 6 slices were fixed on the boundaries of the 3D slab. Spatial-spectral encoding is performed in *k*-space, where three orthogonal gradients and the evolution of time traverse a path in four dimensions (k_x, k_y, k_z, *t*), the Fourier space corresponding to (*x, y, z, f*). Here *x* and *y* are the transverse coordinates, *z* is the slice selection direction, and *f* is the chemical shift. k_y and k_z are sampled on a uniform spatial grid by phase encoding prior to readout. k_x and *t* are sampled simultaneously during the readout interval on a zig-zag trajectory defined by a periodic trapezoidal gradient (Fig. 1). Acceleration was performed by subsampling uniformly the *k*-space data along the k_y and k_z dimensions by factors R_y and R_z, respectively. The acquisition time is then given by $T_A = N_y/R_y \times N_z/R_z \times T_R$. Three in vivo accelerations were employed: R = 4 (R_y = 2, R_z = 2), R = 8 (R_y = 4, R_z = 2), and R = 12 (R_y = 6, R_z = 2). For comparisons the fully sampled data were also acquired. Data acquisition includes WS and non-WS (NWS) scans. Data were acquired
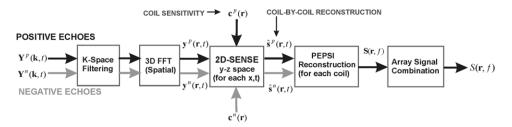
FIG. 2. SENSE-PEPSI reconstruction diagram. Multicoil accelerated positive $\mathbf{Y}^p(\mathbf{k}t)$ and negative $\mathbf{Y}^n(\mathbf{k}t)$ echoes are reconstructed separately using 2D-SENSE reconstruction for each timepoint. Coil-by-coil PEPSI reconstruction is then performed where positive and negative echoes are combined after spectral phase correction. The final spectroscopic image $S(\mathbf{r},f)$ data is obtained by least-squares combination of the coil-by-coil reconstruction.

in an axial orientation using a $32 \times 32 \times 8$ spatial matrix to reconstruct 8 axial slices (FOV: $240 \times 240 \times 100$ mm, nominal voxel size: 0.7 cc). The readout direction was right-left (RL) and phase-encoding directions were anterior-posterior (AP) and foot-head (FH). Fully sampled data were acquired in 8.5 min using TR = 2 sec, TE = 15 ms. The readout gradient consisted of 512 periods (each period has a positive and negative part). The spectral bandwidth after positive and negative echo separation was 1087 Hz. A second NWS scan with much shorter readout duration (16 periods) and TR = 500 msec was acquired to estimate coil sensitivity profiles (2.1 min). Data were collected with 2-fold oversampling for each readout gradient separately to improve regridding performance and using a ramp sampling delay of 8 μs to limit chemical shift artifacts. Regridding was applied to correct for ramp sampling distortion of the k_x-t trajectory. After regridding, 2-fold oversampling was removed. The datasets were filtered in k-space using a regular Hamming window along the x and y dimensions, which increased the effective voxel size to 1.8 cc.

SENSE-PEPSI Reconstruction

SENSE-PEPSI reconstruction was performed on the accelerated NWS and WS data by separate processing of echoes acquired with positive and negative gradients (Fig. 2). The NWS dataset is required as a reference for spectral phase correction, frequency alignment, eddy current correction, and absolute metabolite concentration estimation. Accelerated positive and negative echoes ($\mathbf{Y}^p(\mathbf{k}t)$ and $\mathbf{Y}^n(\mathbf{k}t)$, respectively, where $\mathbf{k} = (k_x, k_y, k_z)$ is the k-space vector) were sorted into separate arrays after time reversal of the data acquired with negative gradients. A spatial Fourier transform was then applied to obtain the spatially aliased signals $\mathbf{y}^p(\mathbf{r}t)$ and $\mathbf{y}^n(\mathbf{r}t)$, where $\mathbf{r} = (x,y,z)$ is the position vector. 2D-SENSE reconstruction with regularization as described below was applied to each timepoint of $\mathbf{y}^p(\mathbf{r}t)$ and $\mathbf{y}^n(\mathbf{r}t)$ to remove aliasing along y and z. Coil-by-coil SENSE reconstructions were computed by multiplying the 2D-SENSE reconstruction by each of the individual coil profiles ($\mathbf{c}^p(\mathbf{r})$ for positive echoes and $\mathbf{c}^n(\mathbf{r})$ for negative echoes) to obtain $\hat{\mathbf{s}}^p(\mathbf{r},t)$ and $\hat{\mathbf{s}}^n(\mathbf{r},t)$. PEPSI reconstruction (7,8) was performed using the coil-by-coil SENSE reconstruction, where the unfolded WS data from each coil was separately phase-corrected and frequency-aligned along the spectral domain using the corresponding unfolded NWS dataset for coherent combination. Zero-order phases of the water signals were automatically determined in the

unfolded NWS data, and these phase corrections were applied to the corresponding unfolded WS data arrays. Spectral frequency assignment in the unfolded WS array was made using the unfolded NWS data and assuming that the largest signal in the unfolded NWS data represents water. Positive and negative echo data were then added. Eddy-current correction (33) was applied to the reconstructed NWS and WS data using the phase of the reconstructed NWS data to remove residual line shape distortion and possible water sidebands. The resulting multicoil spatial-spectral signal $\mathbf{S}(\mathbf{r},f)$ was then combined using a least-squares combination, i.e., SENSE reconstruction for the case of nonaccelerated data, to obtain the final spectroscopic image $S(\mathbf{r},f)$:

$$S(\mathbf{r},f) = \frac{\displaystyle\sum_{l=1}^{N_c} c_l{}^*(\mathbf{r}) S_l(\mathbf{r},f)}{\displaystyle\sum_{k=1}^{n} c_l{}^*(\mathbf{r}) c_l(\mathbf{r})}, \qquad [1]$$

where $S_l(\mathbf{r},f)$ is the reconstructed signal for the *l-th* coil, $c_l(\mathbf{r})$ is the coil sensitivity, and * denotes complex conjugation.

2D-SENSE with SSVD Solution

2D-SENSE reconstruction was performed on the *y-z* space for each point of the *x-t* space. The x and t-space are considered to be orthogonal, since the chemical shift artifact of the PEPSI spatial-spectral encoding is small (8). Correlation between coils was removed by prewhitening the acquired data and the estimated coil sensitivity functions using a sample average estimate of the noise covariance matrix (24). The benefit of this operation is that the noise covariance matrix becomes equal to identity and can hence be omitted later in the reconstruction. From this point onward we consider that the accelerated data and the reference data to estimate the coil sensitivity functions were prewhitened, thus creating a set of virtual channels that are uncorrelated.

The signal acquired by each coil in k-space with uniform subsampling (acceleration) of k_y and k_z by factors R_y and R_z respectively can be represented as:

$$Y_l(k_x, k_y, k_z) = \sum_{x,y,z} s(x,y,z) c_l(x,y,z) e^{j2\pi(k_x x + R_y k_y y + R_z k_z z)},$$

$$l = 1,2, \ldots, N_c, \quad [2]$$

where $s(x,y,z)$ is the object function to be reconstructed, $c_l(x,y,z)$ is the coil sensitivity function and N_c is the number of coils. Applying a spatial discrete Fourier transform (DFT), we obtain the spatially aliased signals:

$$y_l(x,y,z) = \sum_{m_y=0}^{R_y-1} \sum_{m_z=0}^{R_z-1} s(x, y + m_y\hat{W}_y, z + m_z\hat{W}_z)c_l(x,y + m_y\hat{W}_y, z + m_z\hat{W}_z), \quad [3]$$

where $\hat{W}_y = W_y/R_y$ and $\hat{W}_z = W_z/R_z$ are the reduced FOV along y and z (W_y and W_z represent the full FOV). Concatenating the signals acquired by each coil in a column vector $\mathbf{y}$ ($N_C \times 1$), the matrix formulation of the encoding equation with 2D acceleration for each point in the aliased images is given by:

$$\mathbf{y} = \mathbf{Es}, \quad [4]$$

where the entries of the encoding matrix $\mathbf{E}$ ($N_c \times R_yR_z$) are given by the coil sensitivity functions at the corresponding positions indicated in Eq. [4] and the vector $\mathbf{s}$ ($R_yR_z \times 1$) are the set of voxels to be reconstructed. The standard solution of the system is given by the Moore-Penrose pseudoinverse: $\hat{\mathbf{s}} = \mathbf{E}^{\dagger}\mathbf{y} = (\mathbf{E}^H\mathbf{E})^{-1}\mathbf{E}^H\mathbf{y}$ (11). We will refer to this expression as the least-squares (LS) or the standard SENSE solution. For high acceleration, E becomes ill-conditioned and the standard SENSE solution is very susceptible to noise amplification and residual aliasing errors due to numerical instabilities.

In this work we propose an inverse regularization method based on constraining the singular value decomposition (SVD) of the encoding matrix $\mathbf{E}$ to compute its pseudoinverse. The SVD of $\mathbf{E}$ is given by $\mathbf{U}_E\mathbf{\Sigma}_E\mathbf{V}_E^H$, where $\mathbf{U}_E$ ($N_c \times N_c$) and $\mathbf{V}_E$ ($R \times R$) are unitary matrices containing the singular vectors $\mathbf{u}_i$ and $\mathbf{v}_i$ in their columns. $\mathbf{\Sigma}_E$ is a diagonal matrix ($N_c \times R$) containing the singular values of $\mathbf{E}$ (σ_i). The SVD-based pseudoinverse of $\mathbf{E}$ is then given by $\mathbf{E}^{\dagger} = \mathbf{V}_E\mathbf{\Sigma}_E^{-1}\mathbf{U}_E^H$ and the SENSE-SVD solution is represented as:

$$\hat{\mathbf{s}}_{SVD} = \mathbf{V}_E\mathbf{\Sigma}_E^{-1}\mathbf{U}_E^H\mathbf{y} = \Sigma_{i=1}^R \frac{\mathbf{u}_i^H\mathbf{y}}{\sigma_i}\mathbf{v}_i. \quad [5]$$

The SVD and the standard SENSE solution are equivalent. Note that small values of σ_i represent potential numerical instabilities in the reconstruction. Since small singular values will be inverted to large values, either noise or systematic errors in sensitivity estimation affecting the singular vectors associated with these small singular values will be amplified in the reconstruction, resulting in a decreased SNR and residual aliasing artifacts. This situation is particularly evident in regions with overlapped and/or low-value coil sensitivities where the coils are not able to provide distinct information and the reconstruction fails to remove the aliasing. If the number of singular values is high, the truncated SVD solution (34) could be used to eliminate the components responsible for noise and error propagation by setting a minimum singular value threshold. However, for SENSE we have only R singular

values, commonly R < 10, therefore it is not possible to separate those components. Instead of truncating the SVD, the set of singular values can be shifted away from zero using a shift value given by a small portion of the largest singular value, thus the solution components for large singular values will remain similar to the nonshifted SVD while the components corresponding to small singular values will be attenuated. The shifted-SVD (SSVD) approach shifts the set of singular values away from zero using a minimum singular value shift based on an upper bound on the condition number (CN) of $\mathbf{E}$ (c_0). The shifted singular values are given by: $\sigma_i^s = \sigma_i + \Delta\sigma = \sigma_i + \sigma_{max}/\sigma_0$, where σ_{max} is the largest eigenvalue. The condition number is the ratio of the maximum to the minimum singular value. In this way the set of singular values will be shifted away from zero by adding a minimum singular value to improve the conditioning of $\mathbf{E}$. The SSVD of E is then $\mathbf{E}_S = \mathbf{U}_E\mathbf{\Sigma}_E^s\mathbf{V}_E^H$ where $\mathbf{\Sigma}_E^s$ is a diagonal matrix with the shifted singular values. Note that $\mathbf{E}_S$ is a shifted version of $\mathbf{E}$. Since we have a large condition number (CN) for an ill-conditioned matrix, e.g., CN > 1000, and c_0 is chosen in the range of a well-conditioned matrix, e.g., 10 < c_0 < 100, the shift is very small for the largest singular values but it is significant for the small singular values that are responsible for numerical instabilities. If the encoding matrix is well-conditioned, e.g., CN = 5, the $\mathbf{E}_s$ remains very close to $\mathbf{E}$. The SENSE-SSVD solution is given by:

$$\hat{\mathbf{s}}_{SSVD} = \mathbf{V}_E\sum_E^{s-1}\mathbf{U}_E^H\mathbf{y} = \sum_{i=1}^R \frac{\mathbf{u}_i^H\mathbf{y}}{\sigma_i + \Delta\sigma}\mathbf{v}_i. \quad [6]$$

Note that the method acts like a filter, attenuating more the effect of small singular values. For example, assuming that $c_0 = 50$, then $\Delta\sigma = 0.02 \times \sigma_{max}$. For components with $\sigma_i > 0.2\sigma_{max}$, the difference will be less than 10%. Components with $\sigma_i \approx \Delta\sigma$ will be attenuated by a factor of 2. Since small singular values correspond to more oscillatory singular vectors, the method is attenuating fine details in the reconstructed image. Therefore, with SSVD regularization we are improving the SNR and reducing the aliasing artifact at the expense of blurring in regions susceptible to numerical instability. The difference between the SVD and the SSVD solution is given by:

$$\hat{\mathbf{s}}_{SVD} - \hat{\mathbf{s}}_{SSVD} = \sum_{i=1}^R \frac{\Delta\sigma}{\sigma_i}\frac{\mathbf{u}_i^H\mathbf{y}}{\sigma_i + \Delta\sigma}\mathbf{v}_i, \quad [7]$$

Note that for components with large singular values and therefore small $\Delta\sigma/\sigma_i$, the difference is very small.

Array geometry related noise amplification in the reconstruction was computed using the g-factor (11):

$$g(\mathbf{r}) = \sqrt{(\mathbf{E}_S{}^H\mathbf{E}_S)_r^{-1}(\mathbf{E}_S{}^H\mathbf{E}_S)_r}. \quad [8]$$

The regularization procedure will reduce g-factor since it improves the conditioning of the matrix $\mathbf{E}$ and consequently of $\mathbf{E}^H\mathbf{E}$ at the expense that certain features will be omitted in the reconstructed image, e.g., blurring in positions with strongly overlapped coil sensitivities. There-

fore, it allows a tunable tradeoff between ideal accuracy and practical image quality and SNR. To choose the threshold on CN, the reconstruction of the first time-domain point of the accelerated NWS was employed for different values of c_0 between 10 and 100 with steps of 5. The value of c_0 that proportioned the smallest root mean square error (RMSE) was chosen. The RMSE is defined with respect to the nonaccelerated data. For optimal results, c_0 needs to be reoptimized for each geometry/subject, which does not represent an increase in acquisition time, only extra processing time. For the matrix size used in this work it took less than 1 min.

Coil Sensitivity Estimation

Coil sensitivity functions were estimated using spectral water images from an extra fully sampled NWS acquisition with fewer timepoints (17). The reference signal is appropriate since it was acquired with the same readout as the accelerated PEPSI data, which is advantageous to avoid spatial registration errors. Following the inverse Fourier transform law, the integral along the spectral domain is contained in the first temporal point, which was used as the spectral water image for each coil. The change in contrast due to a shorter TR and anatomical features were reduced by normalizing the reference signal of each coil by the sum-of-squares (SoS) reconstruction of the multicoil reference data. The raw sensitivity maps are still impaired by noise and present discontinuities at the object border. Refinement of the raw sensitivity maps was performed by extracting the low-frequency components using polynomial fitting and spatial extrapolation beyond the borders of the object (11). A third order polynomial fit was employed.

Low Spatial-Resolution Effects

Reconstruction from truncated *k*-space data can be represented as the convolution of the true object function and the PSF of the reconstruction method. The PSF is a spatial weighting function that describes the signal origin in that voxel. This aspect is particularly important for MRSI, where the intrinsically low SNR requires a minimal voxel size, or equivalently a maximal sampled spatial frequency, resulting in truncation artifacts and a poor PSF. For truncated *k*-space data sampled at the Nyquist rate (no acceleration), the PSF limits the spatial resolution of the reconstructed image to its effective width and produces Gibbs ringing due to its oscillatory nature. In MRSI, ringing can produce strong contamination from lipid components located at the periphery of the brain, which have a much larger concentration than the metabolites of interest. For parallel imaging, where truncated *k*-space data are sampled at a multiple of the Nyquist rate, the PSF will be also aliased, which may cause residual aliasing artifacts in regions where the coil sensitivities are not well defined (35). For example, due to the low spatial resolution of MRSI the coil sensitivities are poorly defined at the periphery of the brain, where the lipids are located, which cause extra lipid contamination inside the brain due to improper unaliasing of the PSF. Coil sensitivity extrapolation following the third order polynomial fit was performed to avoid discontinuities at the border of the object.

Moreover, the regularization method described above will reduce the effect of inconsistencies between the extrapolation model and the actual coil sensitivities, thus providing an improved PSF. Data truncation effects for SENSE reconstruction were evaluated by computing the PSF. The PSF was computed by reconstructing a simulated source point at a specific spatial position using coil sensitivity profiles estimated with a $128 \times 128 \times 32$ spatial grid to have 4 points along each dimension within each voxel. No spatial filter was employed to reconstruct the PSF.

Spectral Fitting, Metabolite Images, and Error Quantification

Spectra were quantified using LCModel fitting (36). Basis sets included the following 18 metabolites: aspartate (Asp), glutathione (GSH), inositol (Ins), scyllo-inositol (sIns), glucose (Glc), choline (Cho), phosphocholine (PCho), glycerophosphocholine (GPC), creatine (Cr), phosphocreatine (PCr), glutamine (Gln), glutamate (Glu), gamma-aminobutyrate (GABA), N-acetyl-aspartate (NAA), N-acetyl-aspartylglutamate (NAAG), lactate (Lac), phosphoethanolamine (PE), and taurine (Tau). The basis sets for LCModel were generated by simulating the spectral pattern of each metabolite using density matrix simulations based on chemical-shift and J-coupling values (37). The PEPSI sequence was approximated as a simple spin-echo sequence without slice-selective gradients and assuming infinitely short RF pulses.

Spectra were fitted in the spectral range between 1.0 and 4.0 ppm. Metabolic concentration values in the reconstructed WS data were computed in reference to the NWS data using the water-scaling method with the following scale factors: water concentration = 55 molar and attenuation correction for water and metabolites = 1.0. Combined absolute concentrations in millimolar (mM) units are reported in this work: NAA = NAA+NAAG, Cr = Cr+PCr, and Glu = Glu+Gln. Cho was represented by GPC only. Metabolite concentrations were corrected for relaxation effects as described (8).

Errors in metabolite quantification in LCmodel (%SD) are expressed in Cramer-Rao lower bound (CRLB, the lowest bound of the standard deviation of the estimated metabolite concentration expressed as percentage of this concentration), which when multiplied by 2.0 represent 95% confidence intervals of the estimated concentration values (36).

Metabolite concentration images with the spatial matrix of the acquisition ($32 \times 32 \times 8$) were created using the following thresholds to accept voxels: 1) CRLB $\leq$ 20% for NAA and Cr, CRLB $\leq$ 30% for Cho, and CRLB $\leq$ 50% for Glu, and 2) spectral linewidth (FWHM) $\leq$ 0.2 ppm. Error maps were computed between the accelerated data reconstruction and the fully sampled data reconstruction using the root mean square (RMS) value of the difference. Finally, the metabolite concentration maps were interpolated to a $128 \times 128 \times 8$ matrix using zero-filling to improve visualization.

Lipid images were created by spectral integration between 0.5 and 1.6 ppm of the reconstructed absorption mode spectra.
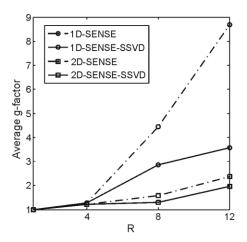
FIG. 3. Average g-factor for simulated 1D and 2D accelerations using the estimated sensitivity maps. For SENSE-SSVD (shifted singular value decomposition), a threshold $c_0 = 25$ on the condition number of the encoding matrix was employed.

RESULTS

SSVD Reconstruction and g-Factor

The g-factor obtained from 1D acceleration was reduced considerably by 2D acceleration (Fig. 3). As a result, the average SNR decrease given by $\bar{g}\sqrt{R}$ where $\bar{g}$ is the average g-factor for R = 8 × 1 is 12.6 but only 4.4 for R = 4 × 2. Therefore, there is a 2.8-fold gain in average SNR performance when using 2D-SENSE for an 8-fold acceleration. However, for high accelerations (R = 4 × 2 and R = 6 × 2), g-factor still presented large values at central zones (Fig. 4a). SSVD reconstruction reduced g-factor for R = 4 × 2 and R = 6 × 2 specially in central zones where the coil sensitivities have low value and overlap, thus producing an ill-conditioned encoding matrix. The threshold of $c_0 = 25$ on the condition number of the encoding matrix represented a good tradeoff to achieve both reasonable numerical conditioning and good unaliasing performance. For R = 2 × 2 the encoding matrix was well-conditioned and

therefore the SSVD solution did not affect the reconstruction. Even though SENSE-SSVD provided low and more uniform g-factors at high accelerations, the SNR penalty due to highly undersampled data ($\sqrt{R}$-factor) imposed the limit for the maximum feasible acceleration. SENSE-SSVD reconstruction of the first time-domain point of the accelerated NWS data presented good performance up to R = 4 × 2 (Fig. 4b). For R = 6 × 2, the reconstruction was deteriorated due to high acceleration factor along the y dimension.

Point Spread Function

2D-SENSE reconstruction of the accelerated data with coil sensitivity extrapolation beyond the border of the brain provided a properly unaliased PSF (Fig. 5). Without sensitivity extrapolation, SENSE reconstruction may lead to residual aliasing artifacts due to discontinuities at the object border. The SSVD solution improved aliasing suppression for larger accelerations (R = 4 × 2 and R = 6 × 2). The aliasing peaks along the y dimension were reduced by 35 dB approximately for $R_y = 2$ and $R_y = 4$. For $R_y = 6$, the aliasing peak to the left of the signal peak was poorly suppressed if the SSVD was not used. With SSVD the aliasing peaks for $R_y = 6$ were at least reduced by 20 dB. The aliasing peak along the z dimension was reduced by 20 dB approximately for $R_z = 2$. The PSF for SENSE reconstruction is asymmetric which is due in part to asymmetries in the array coil configuration. Note that for R = 1 × 1 (nonaccelerated data), the PSF for SENSE reconstruction presented lower side lobes than the one for SoS reconstruction, which results in reduced contamination from outside voxels. This is due to the better defined coil sensitivity functions used in SENSE. For SoS reconstruction, coil sensitivities are assumed to be equal to the spatial SNR profiles of the data; for SENSE a polynomial fit was employed.

Metabolite Maps and Spectra

Metabolite concentration mapping was feasible up to R = 4 × 2 (1-min acquisition) with a moderate reduction in
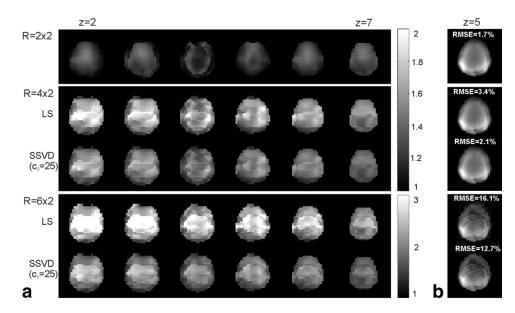

FIG. 4. **a:** g-factor maps for slices 2–7 and **b:** reconstruction of the first time-domain point of the NWS data from slice 5 for different accelerations. The threshold on CN was set using the reconstruction with R = 4 × 2 ($c_0 = 25$). RMSE is the average RMS error with respect to the nonaccelerated data (R = 1 × 1). Note the reduction of g-factor for the SSVD reconstruction, which reduces noise in the reconstructed spectra. R = 2 × 2 and R = 4 × 2 presented similar reconstruction to the nonaccelerated data. For R = 6 × 2, even though the g-factor was reduced considerably using SSVD reconstruction, the SNR reduction due to $\sqrt{R}$-factor deteriorated the reconstruction.
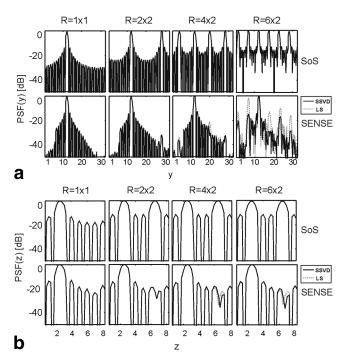
FIG. 5. Point spread function (PSF) along *y* (**a**) and *z* (**b**) for different accelerations. The source point was located at the border of the brain, where there is a discontinuity of the reference signal to estimate the coil sensitivities. The top row shows the aliased PSF for SoS reconstruction of the accelerated data and the bottom row the unaliased PSF for SENSE reconstruction. Note that the reconstruction using SSVD presented better aliasing suppression.

contamination that could have happened due to residual aliasing was highly reduced by extrapolation of the sensitivity maps and the SSVS reconstruction. Figure 9a shows lipid maps for slice 5 from the nonaccelerated data (R = 1 × 1) and R = 4 × 2 using standard SENSE (LS) and SSVD reconstruction. Accelerated data reconstruction showed lipid contamination due to residual aliasing especially in central zones where the encoding matrix is ill-conditioned as shown in the g-factor maps in Fig. 4a. On average the lipid contamination in standard SENSE reconstruction was reduced by a factor of 1.6 when using SSVD reconstruction due to improved unaliasing of the PSF. Figure 9b shows an example from a white matter region where the lipid contamination was reduced by a factor of 1.8.

DISCUSSION

In this work we demonstrated feasibility of a very high-speed method for volumetric spectroscopic imaging in human brain using a combination of highly accelerated PEPSI and 2D-SENSE with a 32-element array coil. We show that the acquisition of short TE (15 ms) 3D-PEPSI with a 32 × 32 × 8 spatial matrix can be accelerated up to 1 min to map the concentrations of NAA, Cr, Cho, and Glu at the expense of a moderate reduction in spatial-spectral quality. This short acquisition time constitutes a major advance as compared to previous studies using parallel MRSI, such as data presented in Ref. 16 that required 20 min of encoding time for the same spatial matrix. Large accelerations in parallel imaging comes with a spatially
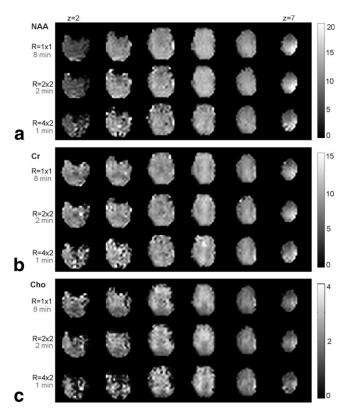
spatial-spectral quality when compared to the nonaccelerated acquisition: RMSEs were less than 0.3%; and the increase in average CRLBs were 5.1, 6.8, 10.7, and 13.9 for NAA, Cr, Cho, and Glu, respectively (Fig. 8a). R = 2 × 2 (2-min acquisition) presented similar results to the nonaccelerated acquisition: RMSEs were less than 0.5%; and the increase in average CRLBs were 2.0, 2.5, 5.6, and 5.4 for NAA, Cr, Cho, and Glu, respectively (Fig. 8b). Figure 6 shows the concentration maps for the three major single resonances NAA, Cr, and Cho. Figure 7a shows the corresponding results for Glu (a multiplet resonance with comparatively low sensitivity). Table 1 shows average concentration values for each acceleration, which are within the range of concentration values reported in previous studies (38). The inferior slices (2 and 3) suffered from larger errors since the coil sensitivities are lower in those brain regions. The accuracy of spectral quantification, indicated by the CRLB from LCModel fitting, decreased with acceleration due to reduced SNR (Fig. 8b). This situation is particularly evident in the inferior slices for the reason mentioned above. The Glu image shows similar intensity in central and lateral gray matter (GM), and much lower intensity in white matter (WM) ($\approx$50% less in the voxel from Fig. 7a), consistent with previous studies (ratio Glu(GM)/Glu(WM) = 2.4±0.5 (38)). Examples of spectra show decreased SNR with larger acceleration, as expected, and small distortions around the lipid region (1.3 ppm) due to imperfections in the estimation of coil sensitivity information at the periphery (Fig. 7b). However, extra lipid

FIG. 6. Metabolite concentration maps of (**a**) NAA, (**b**) Cr, and (**c**) Cho for slices 2–7.

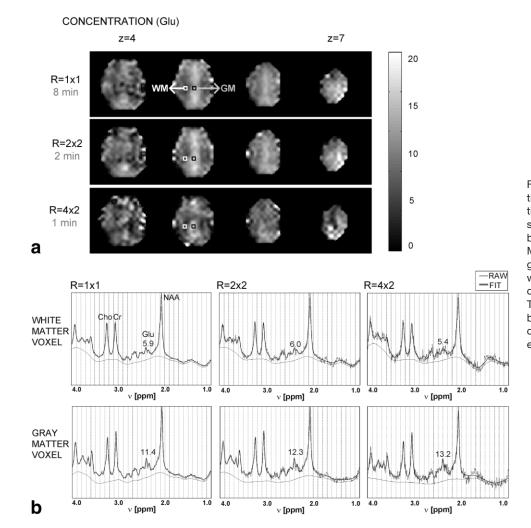CONCENTRATION (Glu)

a

b

FIG. 7. **a:** Glutamate concentration maps at different accelerations for slices 4–7. **b:** Raw absorption mode spectrum (thin black line) and corresponding LC-Model fit (bold black line) for a gray matter (GM) voxel and a white matter (WM) voxel (voxel locations are indicated in part **a**). The remaining baseline is given by the smooth curve. The concentration of glutamate is given in each case.

varying reduction in SNR, which is due to the acquisition of fewer phase encoding steps ($\sqrt{R}$-factor) and noise amplification in the reconstruction due to ill-conditioning of the encoding matrix (g-factor) (11). A high acceleration factor (R = 8) was achieved by using 2D acceleration ($R_y = 4$ and $R_z = 2$), a large array coil of 32 elements and regularization in the SENSE reconstruction.

Acceleration applied simultaneously to the k_y and k_z phase-encoding dimensions increased the acceleration capability by reducing the large SNR loss from high 1D accelerations. The conditioning of the reconstruction improved considerably by exploiting sensitivity encoding

along two dimensions and therefore reduced geometry related noise amplification as described in Ref. 21. The difference between 1D-SENSE and 2D-SENSE for the same net acceleration factor is given by the g-factor. 2D-SENSE presents a lower and more spatially uniform g-factor than 1D-SENSE (see Figs. 3, 4). For example, the average SNR decrease for R = 8 × 1 is 12.6 but only 4.4 for R = 4 × 2. Therefore, there is a 2.8-fold gain in average SNR performance when using 2D-SENSE in this work for an 8-fold acceleration.

Even though the combination of the 32-element array and 2D acceleration improved the conditioning of the en-

FIG. 8. **a:** RMS error of the concentrations of NAA, Cr, Cho, and Glu from the accelerated data reconstruction with respect to the acceleration factor. The RMSE is computed with respect to the concentration of the fully sampled data reconstruction. **b:** Spectral fitting error given by the average CRLB (Cramer-Rao lower bound) from LCModel fitting with respect to the acceleration factor for NAA, Cr, Cho, and Glu.
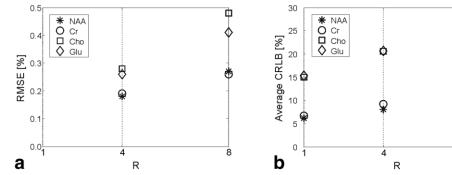

a

b

Table 1
Average Absolute Concentration and Standard Deviation for Different Accelerations

Metabolite	Absolute concentration [mM]		
	R = 1 × 1	R = 2 × 2	R = 4 × 2
NAA	9.2 ± 3.4	9.4 ± 3.8	9.5 ± 4.3
Cr	7.3 ± 2.4	7.2 ± 2.2	7.2 ± 2.8
Cho	1.6 ± 0.7	1.4 ± 0.8	1.4 ± 0.9
Glu	8.3 ± 3.6	8.5 ± 3.9	8.8 ± 5.2

coding matrix, the g-factor was still high in positions with low value and overlapped coil sensitivities. When the sensitivities of the receiver coils severely overlap, different rows of the encoding matrix become nearly identical. This causes the encoding matrix to become nearly singular and therefore highly susceptible to amplify noise and errors in the coil sensitivities estimation process associated with small singular values. Regularization of the encoding matrix inversion can be performed by constraining the SVD solution. One possible strategy is to truncate the singular values that are lower than a certain threshold. This solution, known as truncated SVD, can be applied when the encoding matrix is sufficiently large so that the fraction of eigenvalues retained still provides a reasonable approximation to the true solution, e.g., SPACE-RIP method (34). For SENSE, a small encoding matrix is used for each position in the aliased images, therefore the number of singular values is very small and truncated SVD is not an adequate approach. In this work we proposed the SSVD solution, which consists of shifting the set of singular values of the encoding matrix away from zero based on a threshold on the condition number (SSVD solution). The method proved to work adequately for SENSE to improve the conditioning of the encoding matrix in positions with low value and overlapped coil sensitivities at the expense of spatial resolution in central regions of the reconstructed image. Since MRSI is intrinsically a low spatial resolution technique, this effect is small. The SSVD was tuned using the first time-domain point of the NWS data (maximum SNR), and the same procedure was applied to later timepoints which are noisy.

The analysis of the PSF revealed the parameters to optimize the sensitivity estimation process. The use of sensitivity extrapolation beyond the borders of the object highly reduced the aliasing peak from positions close to the border of the brain, consistent with previous findings (12), and SSVD reconstruction provided better aliasing suppression at large acceleration factors for positions with overlapped coil sensitivities. These two factors were very important to reduce extracranial lipid contamination due to residual aliasing. Lipid signals are particularly strong at short TE, which is advantageous to maintain the sensitivity advantage at high field and to improve the detection of J-coupled metabolites. The sensitivity profiles were fitted using a third-order polynomial function, which provided a better representation of this array coil than the commonly used second-order polynomial function. SSVD reconstruction reduced the lipid contamination inside the brain as compared to standard SENSE reconstruction by a factor of 1.6 on average due to better aliasing suppression in regions with overlapped coil sensitivities.

The maximum attainable acceleration was evaluated quantitatively using the RMSE of the metabolite concentration with respect to the nonaccelerated acquisition and the CRLB from LCModel spectral fitting. The CRLB represents the combined influence of SNR, spectral line width, and spectral shape on the accuracy of the fit. We also generated RMSE maps to evaluate qualitatively the spatial homogeneity of the concentration maps. Based on these parameters, R = 4 × 2 presented an acceptable reduction in spatial-spectral quality to map the concentrations of NAA, Cr, Cho, and Glu.

The short acquisition time of the method is advantageous for applications using hyperpolarized contrast agents (39), allowing highly accelerated acquisition of large data volumes during the short duration of enhanced polarization. Also, the use of high magnetic field strength has been shown to improve the performance of parallel imaging by increasing the baseline SNR and providing stronger sensitivity encoding (22). These two factors promise to shift the SNR balance for highly parallel MRI and perhaps pay the price for even larger array coils. In future work we are planning to implement the technique at 7 T using a 32-element array. However, in order to take advantage of the larger acceleration capability and to achieve adequate volume coverage for 3D acquisitions it is necessary to maximize the uniformity of the spectral quality using improved volumetric shim algorithms and automatic placement of the OVS slices. We are in the process of implementing automatic positioning of the OVS slices for 3D experiments using lipid masks from high-resolution images (40).

In conclusion, this work extended our previously introduced PEPSI-SENSE method (17) for fast 3D-MRSI. A high 2D acceleration was achieved by using a large array coil
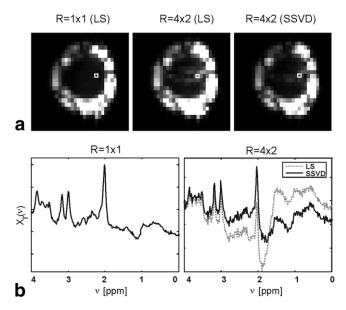

FIG. 9. **a:** Lipid image from slice 5 for R = 1 × 1 and R = 4 × 2 using standard SENSE (LS) and SSVD reconstruction. **b:** Absorption mode spectrum from the voxel indicated in part **a**. Note the reduction in lipid contamination due to residual aliasing in areas with high g-factor seen in Fig. 4b when using SSVD reconstruction as compared to standard SENSE reconstruction.

and SVD-based regularization in SENSE reconstruction. In vivo results demonstrated that single-average 3D-MRSI with a $32 \times 32 \times 8$ spatial matrix and 1.8 cc effective voxel size at 3 T can be accelerated with minimum acquisition time of 1 min. SVD-based regularization in SENSE reconstruction leads to improved conditioning of the reconstruction in regions with low value and overlapped coil sensitivities and thus reduction of lipid contamination inside the brain from peripheral regions. The short acquisition time makes the method suitable for volumetric mapping of metabolites (including J-coupled) as an add-on in clinical MR studies.

ACKNOWLEDGMENTS

REFERENCES

1. Brown TB, Kincaid BM, Ugurbil K. NMR chemical shift imaging in three dimensions. Proc Natl Acad Sci U S A 1982;79:3523–3526.
2. Maudsley AA, Hilal SK. Spatially resolved high resolution spectroscopy by four dimensional NMR. J Magn Reson 1983;51:147–152.
3. Duijn JH, Matson GB, Maudsley AA, Weiner MW, 3D phase encoding ^{1}H spectroscopic imaging of human brain. Magn Reson Imaging 1992; 10:315–319.
4. Pohmann R, von Kienlin M, Haase A. Theoretical evaluation and comparison of fast chemical shift imaging methods. J Magn Reson 1997; 129:145–160.
5. Mansfield P. Spatial mapping of the chemical shift in NMR. Magn Reson Med 1984;1:370–386.
6. Posse S, DeCarli C, Le Bihan D. Three-dimensional echo-planar MR spectroscopic imaging at short echo times in the human brain. Radiology 1994;192:733–738.
7. Posse S, Tedeschi G, Risinger R, Ogg R, Le Bihan D. High speed ^{1}H spectroscopic imaging in human brain by echo planar spatial-spectral encoding. Magn Reson Med 1995;33:34–40.
8. Otazo R, Mueller B, Ugurbil K, Wald L, Posse S. Signal-to-noise ratio and spectral linewidth improvements between 1.5 and 7 Tesla in proton echo-planar spectroscopic imaging. Magn Reson Med 2006;56: 1200–1210.
9. Sodickson DK, McKenzie CA. A generalized approach to parallel magnetic resonance imaging. Med Phys 2001;28:1629–1643.
10. Pruessmann KP. Encoding and reconstruction in parallel MRI. NMR Biomed 2006;19:288–299.
11. Pruessmann KP, Weiger M, Scheidegger MB, Boesiger P. SENSE: sensitivity encoding for fast MRI. Magn Reson Med 1999;42:952–962.
12. Dydak U, Weiger M, Pruessmann KP, Meier D, Boesiger P. Sensitivity encoded spectroscopic imaging. Magn Reson Med 2001;46:713–722.
13. Dydak U, Pruessmann KP, Weiger M, Tsao J, Meier D, Boesiger P. Parallel spectroscopic imaging with spin-echo trains. Magn Reson Med 2003;50:196–200.
14. Zhao X, Prost RW, Li Z, Li SJ. Reduction of artifacts by optimization of the sensitivity map in sensitivity-encoded spectroscopic imaging. Magn Reson Med 2005;53:30–34.
15. Sanchez-Gonzalez J, Tsao J, Dydak U, Desco M, Boesiger P, Pruessmann KP. Minimum-norm reconstruction for sensitivity-encoded magnetic resonance spectroscopic imaging. Magn Reson Med 2006;55:287–295.
16. Dydak U. Parallel spectroscopic imaging. In: Proc 2nd Int Workshop on Parallel MRI, 2004.
17. Lin FH, Tsai SY, Otazo R, Caprihan A, Wald LL, Belliveau JW, Posse S. Sensitivity-encoded (SENSE) proton echo-planar spectroscopic imaging (PEPSI) in human brain. Magn Reson Med 2007;57:249–257.
18. Tsai SY, Caprihan A, Posse S, Lin FH. Comparison of SENSE and GRAPPA reconstruction for proton-echo-planar-spectroscopic-imaging (PEPSI). In: Proc 11th Int Conference on Functional Mapping of the Human Brain, Toronto, Canada, 2005. p s43.
19. Rueckert M, Otazo R, Posse S. GRAPPA reconstruction of sensitivity encoded 2D and 3D proton echo planar spectroscopic imaging (PEPSI) with SNR adaptive recalibrating. In: Proc 14th Annual Meeting ISMRM, Seattle, 2006. p 296.
20. Zhu X, Ebel A, Ji JX, Schuff N. Spectral phase-corrected GRAPPA reconstruction of three-dimensional echo-planar spectroscopic imaging (3D-EPSI). Magn Reson Med 2007;57:815–820.
21. Weiger M, Pruessmann KP, Boesiger P. 2D SENSE for faster 3D MRI. MAGMA 2002;14:10–19.
22. Wiesinger F, Van de Moortele PF, Adriany G, De Zanche N, Ugurbil K, Pruessmann KP. Parallel imaging performance as a function of field strength — an experimental investigation using electrodynamic scaling. Magn Reson Med 2004;52:953–964.
23. de Zwart JA, Ledden PJ, Kellman P, van Gelderen P, Duyn JH. Design of a SENSE-optimized high-sensitivity MRI receive coil for brain imaging. Magn Reson Med 2002;47:1218–1227.
24. Lin FH, Kwong KK, Belliveau JW, Wald LL. Parallel imaging reconstruction using automatic regularization. Magn Reson Med 2004;51: 559–567.
25. Zhu Y, Hardy CJ, Sodickson DK, Giaquinto RO, Dumoulin CL, Kenwood G, Niendorf T, Lejay H, McKenzie CA, Ohliger MA, Rofsky NM. Highly parallel volumetric imaging with a 32-element RF coil array. Magn Reson Med 2004;52:869–877.
26. Sodickson DK, Hardy CJ, Zhu Y, Giaquinto RO, Gross P, Kenwood G, Niendorf T, Lejay H, McKenzie CA, Ohliger MA, Grant AK, Rofsky NM. Rapid volumetric MRI using parallel imaging with order-of-magnitude accelerations and a 32-element RF coil array: feasibility and implications. Acad Radiol 2005;12:626–635.
27. Wright SM, Wald LL. Theory and applications of array coils in MR spectroscopy. NMR Biomed 1997;10:394–410.
28. Sodickson DK, Lee RF, Giaquinto RO, Collins CM, McKenzie CA, Ohliger MA, Grant AK, Willig-Onwuachi JD, Yeh EN, Kressel HY. Depth penetration of RF coil arrays for sequential and parallel imaging. In: Proc 11th Annual Meeting ISMRM, Toronto, Canada, 2003. p 469.
29. Posse S, Cuenod CA, Risinger R, Le Bihan D, Balaban RS. Anomalous transverse relaxation in 1H spectroscopy in human brain at 4 Tesla. Magn Reson Med 1995;33:246–252
30. Hetherington HP, Mason GF, Pan JW, Ponder SL, Vaughan JT, Twieg DB, Pohost GM. Evaluation of cerebral gray and white matter metabolite differences by spectroscopic imaging at 4.1T. Magn Reson Med 1994;32:565–571.
31. Wiggins GC, Triantafyllou C, Potthast A, Reykowski A, Nittka M, Wald LL. 32-channel 3 Tesla receive-only phased-array head coil with soccer-ball element geometry. Magn Reson Med 2006;56:216–223.
32. Ogg RJ, Kingsley PB, Taylor JS. WET a T1–B1-insensitive water suppression method for in vivo localized 1H NMR spectroscopy. J Magn Reson Ser B 1994;104:1–10.
33. Klose U. In vivo proton spectroscopy in presence of eddy currents. Magn Reson Med 1990;14:26–30.
34. Hoge WS, Brooks DM, Madore B, Kyriakos W. On the regularization of SENSE and space-RIP in parallel MR imaging. In: Proc IEEE Int Symp Biomed Imaging (ISBI), 2004. p 241–244.
35. Yuan L, Ying L, Xu D, Liang Z-P. Truncation effects in SENSE reconstruction. Magn Reson Imaging 2006;24:1311–1318.
36. Provencher SW. Estimation of metabolite concentrations from localized in vivo proton NMR spectra. Magn Reson Med 1993;30:672–679.
37. Henry P-G, Marjanska M, Walls JD, Valette J, Gruetter R, Ugurbil K. POCE NMR spectroscopy in strongly coupled systems. Magn Reson Med 2006;55:250–257.
38. McLean MA, Woermann FG, Barker GJ, Duncan JS. Quantitative analysis of short echo time ^{1}H-MRSI of cerebral gray and white matter. Magn Reson Med 2000;44:401–411.
39. Ardenkjaer-Larsen JH, Fridlund B, Gram A, Hansson G, Hansson L, Lerche MH, Servin R, Thaning M, Golman K. Increase in signal-to-noise ratio of >10,000 times in liquid-state NMR. Proc Natl Acad Sci U S A 2003;100:10158–10163.
40. Li T, Martínez-Ramón M, Heileman G, Posse S. Automatic outer volume suppression (OVS) slice placement for proton-echo-planar-spectroscopic-imaging (PEPSI). In: Proc 14th Annual Meeting ISMRM, Seattle, 2006. p 3086.